CloudSat's Cloud Profiling Radar After Two Years in Orbit: Performance, Calibration, and Processing

Simone Tanelli, Stephen L. Durden, *Senior Member, IEEE*, Eastwood Im, *Fellow, IEEE*, Kyung S. Pak, Dale G. Reinke, Philip Partain, John M. Haynes, and Roger T. Marchand

***Abstract*—The Cloud Profiling Radar, the sole science instrument of the CloudSat Mission, is a 94-GHz nadir-looking radar that measures the power backscattered by hydrometeors (clouds and precipitation) as a function of distance from the radar. This instrument has been acquiring global time series of vertical cloud structures since June 2, 2006. In this paper, an overview of the radar performance and status, to date, is provided together with a description of the basic data products and the surface clutter rejection algorithm introduced for the Release 04 data product.**

***Index Terms*—A-train, clouds, CloudSat, radar.**

I. Introduction

A NEW satellite mission, the CloudSat Mission [1], was jointly developed by the National Aeronautics and Space Administration (NASA), the Jet Propulsion Laboratory (JPL), the Canadian Space Agency, Colorado State University, and the U.S. Air Force. CloudSat's payload, the Cloud Profiling Radar (CPR) [2], is the first spaceborne 94-GHz (W-band) radar and is contributing vertical cloud profiles over the globe. CloudSat was launched on April 28, 2006; CPR instrument operations began on June 2, 2006. Since that time, CPR has been acquiring the first-ever continuous global time series of vertical cloud structures and vertical profiles of cloud liquid water and ice content with a 485-m vertical resolution and a 1.4-km antenna 3-dB footprint. Fig. 1 shows the vertical structure of a squall line in the North Atlantic observed on May 20, 2006, immediately after the activation of CPR for a brief checkout test. CPR data are providing valuable information for studies of cloud physics, radiation budget, atmospheric water distribution, and as input to numerical weather-prediction models.

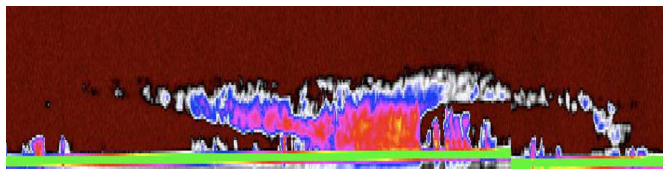

Fig. 1. CPR's first image, May 20, 2006. Vertical section of frontal system in the North Sea. The green band is the ocean surface in the adaptive-height CPR science data window (in color in the electronic version).

In order to take full advantage of observations by other types of spaceborne atmospheric remote-sensing instruments, the CloudSat spacecraft flies in formation as part of the Afternoon Constellation of satellites (also referred to as "A-Train," from Billy Strayhorn's old jazz tune). In particular, CloudSat flies in close formation with CALIPSO [3], which carries a lidar system, so that their respective beams cover the same vertical column within about 15 s.

II. CPR System

CPR is a short-pulse profiling radar; it measures the power backscattered by atmospheric targets (hydrometeors, ice crystals, and cloud droplets) and any other target intercepted by the antenna beam (e.g., the Earth's surface, aircraft, etc.) as a function of time. Time is converted into range based on $r = c_0 t/2$, where c_0 is the speed of light in vacuum. In a normal data-acquisition mode, CPR points at nadir (0.16° off-geodetic nadir since August 15, 2006); therefore, ranging resolves targets in altitude. The narrow antenna beam and the motion of the spacecraft resolve targets in the along-track direction. All CPR products are therefore vertical slices of the troposphere, as shown in Fig. 1. Table I shows some of the main parameters of interest, including the definition of symbols used throughout this paper. The values included in Table I are provided at a higher resolution than the approximate values used throughout the text.

The A-train sun-synchronous orbit covers the latitude ranges between 82.5° S and 82.5° N, with a repeat cycle of 16 days (or 233 orbits). CloudSat reaches its maximum altitude above the Earth's geoid when over Antarctica (about 732 km above sea level) and its lowest altitude when at the equator (about 705 km). CloudSat's reference ellipsoid is the WGS84 for all official products. One vertical profile is acquired for each integration time interval $T_{\mathrm{I}} = 0.16$ s, corresponding to a subsatellite motion of 1.09 km (±10 m, depending on latitude).

Manuscript received February 29, 2008; revised May 19, 2008. Current version published October 30, 2008. This work was supported by the NASA Earth Science Pathfinder Program (ESSP).

S. Tanelli, S. L. Durden, and K. S. Pak are with the Radar Science and Engineering Section, Jet Propulsion Laboratory, California Institute of Technology, Pasadena, CA 91109 USA (e-mail: simone.tanelli@jpl.nasa.gov).

E. Im is with the Earth Science Technology Research and Advanced Concepts Office, Jet Propulsion Laboratory, California Institute of Technology, Pasadena, CA 91109 USA.

D. G. Reinke is with the Cooperative Institute for Research in the Atmosphere, Colorado State University, Fort Collins, CO 80523-1375 USA.

P. Partain is with the METSAT Division, Science and Technology Corporation, Fort Collins, CO 80521 USA, and also with the CloudSat Data Processing Center, Cooperative Institute for Research in the Atmosphere, Colorado State University, Fort Collins, CO 80532-1375 USA.

J. M. Haynes is with the Department of Atmospheric Science, Colorado State University, Fort Collins, CO 80523-1371 USA.

R. T. Marchand is with the Joint Institute for the Study of the Atmosphere and Ocean, University of Washington, Seattle, WA 98195 USA.

Color versions of one or more of the figures in this paper are available online at http://ieeexplore.ieee.org.

Digital Object Identifier 10.1109/TGRS.2008.2002030

TABLE I
CLOUDSAT AND CPR PARAMETERS

Parameter	*Symbol*	Value	Units
Orbit inclination		98.2	deg
Altitude	h_s	705-732	km
Operating frequency	f	94.05	GHz
Pulse width	τ	3.3	μs
Range resolution (6-dB)	Δ_{6dB}	485	m
Antenna diameter	D	1.85	m
Cross-track resolution	Δ_x	1.32-1.38	km
Integration Time	T_I	0.16	s
Along-track res. (in T_I)	Δ_a	1.7-1.72	km
Data window		30	km
Range sampling	Δ_r	239.83	m
Peak power (BOL)	P_t	1820	W
Pulse Rep. Frequency	*PRF*	3700-4300	Hz
Num. of integr. pulses	M	577-679	-
Sensitivity (BOL)	Z_{min}	-30	dBZ

The actual integration of pulses lasts for 96.8% of $T_{\rm I}$ (±0.1%, depending on latitude). The resulting horizontal resolution after integration and including latitudinal dependence is between 1.3 and 1.4 km cross track and between 1.7 and 1.8 km along track (defined at the 6-dB point of the two-way resulting weighting function). This estimate for the along-track resolution replaces the oft-quoted value of 2.5 km, derived early in the program from purely geometrical considerations.

CPR acquires 125 samples per profile, one every ∼240 m. Considering that the spacecraft altitude $h_{\rm s}$ varies with the position along the orbit, the radar timing parameters (including PRF and M) are adjusted based on a lookup table to keep the troposphere inside the 30-km science data window. In particular, the parameters are adjusted so that the Earth's surface return is observed in the data window's lower portion and that a 5–10-km cloud-free region (of the stratosphere) is included in the upper portion. The former provides a useful reference for retrieval algorithms (see, e.g., [4] and [5]), and the latter allows for accurate noise-floor estimation used to perform noise subtraction, and achieve the required minimum detectable reflectivity (or sensitivity).

III. CPR MEASUREMENTS

The discussion on CPR data products presented in this paper is limited to the L1B-CPR [6] and portions of the L2B-GEOPROF [7] data products. The quantities of interest are the calibrated and geolocated parameters used as input to all subsequent atmospheric radar retrieval algorithms.

For volume scattering, the quantity of interest is the radar cross section per unit volume or the radar reflectivity η. From the radar equation [8], η is calculated as

$$\eta = \frac{P_{\rm rec}(4\pi)^3 r^2 L_{\rm a}}{P_{\rm t}\lambda^2 G_{\rm rec} G^2 \Omega \Delta} = C\frac{P_{\rm rec} r^2 L_{\rm a}}{P_{\rm t}} \tag{1}$$

where $P_{\rm rec}$ is the output power of the receiver, $P_{\rm t}$ is the transmitted power, λ is the wavelength, $G_{\rm rec}$ is the receiver gain, G is the antenna gain, r is the range to the atmospheric target, Ω is the integral of the normalized two-way antenna pattern, Δ is the integral of the received waveform shape (proportional to the pulselength $c_0\tau/2$), and $L_{\rm a}$ is the two-way atmospheric loss. CloudSat's L1B product includes the calibrated power input to the receiver ($P_{\rm r} = P_{\rm rec}/G_{\rm rec}$) sampled every 240 m, the radar constant C, and the orbit-averaged estimate of the transmit power $P_{\rm t}$. Reflectivity is then converted (in L2B-GEOPROF) into the equivalent (attenuated) reflectivity factor according to the standard relation

$$Z_{\rm e} = \eta\frac{\lambda^4 10^{18}}{\pi^5 |K_{\rm w}|^2} \tag{2}$$

where $Z_{\rm e}$ has units of $\rm mm^6/m^3$ and is often expressed in decibels as $\mathrm{dB}Z_{\rm e} = 10 * \log_{10}(Z_{\rm e})$. $|K_{\rm W}|^2$ is set to 0.75 (representative for water at 10 °C at the W-band) [9], [10]. CloudSat's L2B-GEOPROF product also includes vertical profiles of $L_{\rm a}$ estimated from the European Center for Medium-Range Weather Forecasts' (ECMWF) auxiliary products.

The second quantity of interest generated within the L1B product is the normalized radar cross section (σ^0) of the Earth's surface, expressed in decibels.

$$\sigma^0 = \frac{P_{\rm rec}(4\pi)^3 r^2 L_{\rm a}}{P_{\rm t}\lambda^2 G_{\rm rec} G^2 \Omega}\frac{1}{\cos(\theta)} = \frac{C\Delta}{\cos(\theta)}\frac{P_{\rm rec} r^2 L_{\rm a}}{P_{\rm t}} \tag{3}$$

where θ is the incidence angle; at nadir, the cosine term can be neglected. This quantity, labeled "Sigma-zero" in the L1B product, is also affected by atmospheric loss. A more detailed discussion on this product is provided later.

CloudSat's data-processing plan included a one-year reprocessing, which has been implemented as planned in 2007. The resulting Release 04 (R04) of the data products includes improvements discussed in the following sections and in the Appendix.

IV. CPR HIGH-LEVEL DESIGN AND PRELAUNCH CALIBRATION

Clouds are weak scatterers of microwave radiation, particularly in contrast to the reflection of the underlying Earth's surface. The overriding requirement on CPR was to achieve a minimum detectable cloud reflectivity factor ($Z_{\rm e}$) of -28 dBZ at the beginning of life (BOL) and -26 dBZ at the end of life (EOL, 22 months after launch). By comparison, the reflectivity for rain is typically 10–50 dBZ; the Tropical Rainfall Measuring Mission (TRMM) precipitation radar (PR) [11] has a sensitivity of around $+17$ dBZ. The CPR required range resolution was 500 m.

In order to achieve such requirements, CPR design and implementation included a high-efficiency antenna assembly (AA), a low-loss quasi-optical transmission line (QOTL), high-power amplifiers [HPA, each one composed of a high-voltage power supply and an extended interaction klystron (EIK)], and a low-noise-figure receiver. CPR is the first of its kind; it demonstrates the W-band application in space of the technologies used for HPA, AA, and QOTL [2].

Absolute calibration of the radar depends on the precise knowledge of r, λ, G, Ω, Δ, $P_{\rm a}$, and $P_{\rm t}$. Prelaunch calibration parameters were obtained from either direct laboratory measurements or analysis of experimental data. The root square

TABLE II
CPR PRELAUNCH CALIBRATION ERROR BUDGET

Parameter	*BOL Budget*	Stability	RSS
Δ	0	0.1	0.1
P_t	1.1	0.4	1.2
$G^2\Omega$	1.0	0.4	1.1
P_r	0.5	0.4	0.6
L_c	0	1.0	1.0
RSS (dB)	1.6	1.2	**2.0**

sum (rss) uncertainty in absolute calibration at BOL, including launch effects, was 1.6 dB. CPR includes two internal measurements (performed every $T_{\rm I}$) to track the stability of the instrument. The receiver gain is measured by a standard hot-/cold-load calibration; the transmitted power $P_{\rm t}$ is measured by a peak detector. The coupling between the detector and the EIK is indicated by a loss factor $L_{\rm c}$ whose stability was budgeted at 1 dB. It was anticipated that the CPR radiometric calibration accuracy, including the uncertainty in stability, would be within 2-dB rss over the life of the mission (Table II).

V. IN-FLIGHT CALIBRATION

Internal measurements show that, to date, both the receiver and the transmitter are performing within the budgeted stability. The receiver gain has been stable within 0.15 dB (peak to peak) since BOL.

As summarized in Table II, the accuracy in the estimation of $P_{\rm t}$ is affected by the coupling $L_{\rm c}$ between the pulse detector and the EIK, via the AA. Considering that the physical path from the AA to the detector is not part of the QOTL and is partially exposed to the sun, $L_{\rm c}$ is more sensitive to changes in the local environment (i.e., position and orientation relative to the Earth and Sun) than the coupling between the transmitter and receiver, via AA and QOTL. As a result, the instantaneous estimates of $P_{\rm t}$ are affected by an orbital fluctuation of 0.7 dB peak to peak (0.2-dB rss); the orbit-averaged estimate of $P_{\rm t}$ (included in all versions of the L1B product) is used in R04 to calculate (1) and (3). Such estimate has been stable within 0.4 dB (peak to peak) since the beginning of the mission. As shown in Section V-B, results of external calibration indicate that $P_{\rm t}$ has actually been stable to significantly better than 0.4 dB and that the observed fluctuation in orbit-averaged $P_{\rm t}$ is determined mainly by a fluctuation in $L_{\rm c}$.

CPR end-to-end system calibration is evaluated by analyzing the measured backscatter of water surface. This method, referred to as external calibration, is widely used in many downward-looking cloud and PRs, both airborne and spaceborne (see, e.g., [12]–[17]). This method and results are described in detail in the next three sections.

A. Measurement and Correction of the Ocean Radar Backscatter

The normalized radar cross section (σ^0) of the Earth's surface defined by (3) is, in practice, calculated as follows:

$$\sigma^0 = P_{\rm rec}(i_{\rm surf}) L_\theta L_{\rm r} \frac{C\Delta}{\cos(\theta)} \frac{r^2 L_{\rm a}}{P_{\rm t}} \tag{4}$$

where $i_{\rm surf}$ is the range bin intersecting the Earth's surface, $P_{\rm rec}(i_{\rm surf})$ is the corresponding power sample, L_θ is the shape factor accounting for the range spreading of the point-target return for nonzero incidence angles [10], [19], and $L_{\rm r}$ is the range-sampling bias documented, e.g., in [19] and [20].

Two types of measurements are discussed here to address the CPR stability and overall calibration, namely, σ^0 measured in the standard nadir-pointing configuration over ocean and in clear air and σ^0 measured during monthly calibration maneuvers when the radar was tilted 10° off-nadir for 5 min each time. The former provides the largest data set and is used to assess CPR stability in time; the latter takes advantage of the relative wind invariance of σ^0 at incidence angles close to 10° and is used to assess the CPR overall calibration accuracy. All data presented herein are obtained with the improved surface clutter estimation (SCE) algorithm described in the Appendix and implemented in L1B processing as of R04.

Of the three loss factors, the atmospheric loss $L_{\rm a}$ is the one that can assume the largest range of values (between about 0.3 and 8 dB in clear-air conditions). The first calibration assessment was completed by estimating the $L_{\rm a}$ from the AQUA/AMSR-E products [21]. The choice of this data set is an immediate consequence of the characteristics of the A-train; AMSR-E estimates are colocated within less than 2 min from CPR measurements at a resolution of 21 km. In [3], the following relationship was applied to obtain the one-way path integrated attenuation (PIA):

$$\mathrm{PIA}_{\rm gas} = a + b \cdot \mathrm{wv} + c \cdot \mathrm{wv}^2 \tag{5}$$

where wv is the columnar amount of water vapor (in millimeters) reported by AMSR-E (nominal rmse is 0.57 mm) and a, b, and c were coefficients obtained from the best fit of the total path attenuation calculated according to Liebe *et al.* [22] from an ensemble of vertical profiles of temperature and water vapor discriminated by their resulting wv. The $\mathrm{PIA}_{\rm gas}$ was then converted to path loss $L_{\rm a}$ accounting for the path incidence angle θ. $L_{\rm a}$ estimates obtained through (5) with the coefficients used in [3] were compared with the L2B-GEOPROF gas attenuation profiles generated from ECMWF reanalysis vertical profiles with a different version of the model by Liebe [23]. The comparison showed a possible overestimation of PIA through (5). However, the bias is small (relative to the uncertainty of water vapor and temperature inputs), with a bias less than 5% for PIA $<$ 3 dB and less than 20% for PIA $>$ 6 dB (typical of water-vapor burdens in moist tropics). Nonetheless, results obtained from scenes where wv is low (e.g., $L_{\rm a} <$ 3 dB) were given priority to assess the CPR calibration. A new set of coefficients has been derived by the regression of ECMWF-derived profiles for the geographical regions, where the monthly calibration maneuvers are performed (i.e., oceanic basins in the southern hemisphere between the equator and 45° S), and for the relevant time of day (calibration maneuvers are always performed during eclipse, in the descending portion of the orbit). These are $a = 0.15$, $b = 0.05$, and $c = 0$. As will be shown in Section V-C, the application of these new parameters to the measurements obtained during the calibration maneuvers resulted in a lower residual sensitivity to the

estimated $L_{\rm a}$, indicating a more reliable correction. Nevertheless, measurements obtained for a large $L_{\rm a}$ are intrinsically affected by larger uncertainties; therefore, for most results, a threshold on $L_{\rm a}$ was imposed. We point out also that "clear air" was defined as no cloud return detected by CPR and AMSR-E-estimated cloud liquid water < 0.2 mm.

The shape factor loss L_θ is one at nadir, representing an ideal beam-limited case. During the monthly 10° calibration maneuvers, the incidence angle θ is about 11.1° (due to the Earth's curvature). Although, at first approximation, this geometry still belongs to a beam-limited case, careful accounting for the temporal spread of the surface target response results in a shape loss of about 1.12 (i.e., approximately $+0.5$ dB). This estimate was derived by analyzing the high-resolution surface target response (described in the Appendix) observed during these maneuvers with the one observed during nadir operation. It is worth noting that the general expression derived in [19] for a Gaussian beam and Gaussian pulse response approximations matches very well the values calculated with the actual CPR pulse response. Using the results in [19], considering that the "flat-earth" approximation cannot be adopted for our geometry, and separating the range-sampling bias from the shape factor loss, we obtain

$$L_\theta = \theta_3 \cdot \sqrt{\theta_3^{-2} + \left(\frac{c\tau}{2r_{\rm surf}}\frac{\cos(\theta)}{\theta}\right)^{-2}} \tag{6}$$

which gives 0.58 dB at an 11.1° incidence under the double Gaussian approximation and assuming that no range-sampling bias is present (accounted for separately by $L_{\rm r}$).

The range-sampling bias $L_{\rm r}$ can assume values ranging from 0 (when the surface bin is sampled at the exact time of intersect) to 1.35 dB (when the surface bin is sampled $\Delta_{\rm r}/2$ away from the time of intersect). $L_{\rm r}$ is estimated by the SCE algorithm as described in the Appendix, with a one-sigma uncertainty ranging from 0.08 (for clear-air profiles over ocean) to 0.12 dB (for profiles over ocean where the return signal from atmospheric targets is more than 10 dB below the return from the surface). As described in the Appendix, whenever the SCE algorithm does not find an acceptable match for the surface return (i.e., in cases where heavy attenuation, multiple-scattering returns, or the shape of the orography within the footprint deteriorate the surface response with respect to the one expected from flat surface), this correction is not applied. The resulting correction applied to obtain the sigma-zero value reported in L1B corresponds to

$$\sigma^0 = P_{\rm rec}(i_{\rm surf}) L_{\rm r} C \Delta \frac{r^2}{P_{\rm t}}. \tag{7}$$

B. Clear-Air Ocean Surface Backscatter at Nadir

Values of σ^0 measured in the standard data-acquisition mode (nadir) were used to monitor the stability of the instrument calibration. At incidence angles close to normal, σ^0 measured in clear air and over water depends mainly on wind speed w, atmospheric loss $L_{\rm a}$, and, to a lesser extent, on sea surface temperature SST. In general, we can write $\sigma_0(\theta, \phi, w, {\rm SST}, S, T_{\rm a}, p, \lambda)$, where θ is the incidence angle, ϕ is the wind azimuth relative to the line of sight, w is the wind speed at the surface, SST is the sea surface temperature, S is the sea water (SW) salinity, $T_{\rm a}$ is the air-temperature profile in the boundary layer, p is the polarization, and λ is the wavelength.

Dependence on salinity is predicted to be negligible at the W-band (i.e., $\ll 0.1$ dB) by three models [24]–[26]; no observation indicates otherwise. Dependence on the air-temperature profile at the air–water interface is also estimated to be a minor contributor by the model described in [27] and is not addressed further here. Dependences on θ, ϕ, and p are irrelevant at nadir, and will be addressed only in the next section.

In general, the quasi-specular contribution (from specular facets) dominates the radar return over ocean for incidence angles below 15°. The most commonly adopted formulation, which has been proven to be quite accurate, assumes an isotropic rough surface with Gaussian statistics (see [15], [28]–[31] and references cited therein) and includes the use of an *effective* reflection coefficient ρ_λ and effective mean-square slope ${\rm mss}_\lambda$

$$\sigma^0_\lambda(\theta) = \frac{\rho_\lambda}{mss_\lambda}\sec^4(\theta) e^{\left(-\frac{\tan^2(\theta)}{mss_\lambda}\right)} \tag{8}$$

where the subscript λ indicates dependence on the operating wavelength. The effective nadir reflection coefficient ρ_λ is defined as

$$\rho_\lambda = |C_\lambda \Gamma(0,\lambda)|^2 \tag{9}$$

where $\Gamma(0,\lambda) = [n(\lambda)-1]/[n(\lambda)+1]$ is the normal incidence Fresnel coefficient, $n(\lambda)$ is the complex index of refraction for seawater, and C_λ is the correction factor accounting for diffraction effects generated by curvatures in the surface at a wavelength smaller than λ. The effective mean-square slope is defined as

$${\rm mss}_\lambda = \int_{|\mathbf{k}|=k_{\rm F}}^{|\mathbf{k}|=k_\lambda} |\mathbf{k}|^2 S(\mathbf{k}) {\rm d}\mathbf{k} \tag{10}$$

where $\mathbf{k}$ is the wavenumber vector, $k_{\rm F}$ is a low-cutoff wavenumber determined by the instrument field of view, k_λ is the high-cutoff wavenumber inversely proportional to the instrument operating wavelength, and $S(\mathbf{k})$ is the directional wave height spectrum. It was therefore predicted that ${\rm mss}_\lambda$ increases with the operating frequency; experimental results have confirmed this interpretation [14].

While a multitude of model functions and experimental results describing $\sigma_0(\theta, \phi, w, {\rm SST}, T_{\rm a}, \lambda)$ have been obtained in the last decades for $\lambda > 8$ mm or λ in the VIS–IR region (see, e.g., [32]–[34]), a significantly smaller amount of work has been performed for the W-band (i.e., $\lambda = 3$ mm), mainly due to the scarcity of experimental data and applications and to the relatively larger uncertainties tied to the correction for $L_{\rm a}$. The pioneering work by Li *et al.* [12] has been used as the main reference for CPR external calibration; in that paper, the authors compared the σ^0 observations obtained by their W-band airborne Cloud Radar System with σ^0 models

developed in the past. Perhaps the major finding of that paper was the confirmation that some of the conclusions drawn for lower frequencies still hold at the W-band; most notably, they confirmed that the region around the 10° incidence angle is characterized by a relative insensitivity to w for w between about 4 and 15 m/s. This result was of paramount importance in the definition of CloudSat's calibration plan (see next section). For this reason, the observed $\langle\sigma^0\rangle$ are, here, compared first to the values predicted by the same models used in [12].

Values of σ^0 measured by CPR and corrected for $L_{\rm a}$ are accumulated for periods of 16 days or more by screening for the following conditions: clear air, $L_{\rm a} < 2$ dB, over ocean (profiles classified as ocean in L1B and with at least two more oceanic profiles on each side to avoid shallow coastal waters), and within $\pm 55°$ latitude (to avoid sea ice). The resulting sample population is binned by w and SST (AMSR-E estimates). Fig. 2 shows the result of this stratification for the May 2007 period; we will first give an overview of the salient results that can be observed therein, and then, we will further compare the measurements with modeled values. The top two panels show the average $\langle\sigma^0\rangle$ and standard deviation std(σ^0) as the function of surface wind w and segregated by sea surface temperature SST (color coded). In general, the wind dependence of $\langle\sigma^0\rangle$ is in good agreement with the models, and the absolute level is within the range of predicted values. The large majority of estimates shows a std(σ^0) of ∼0.5 dB (which can easily be attributed to measurement uncertainties); low wind speeds are associated to larger std(σ^0) due to the increased $d\sigma^0/dw$ sensitivity in that region. We observe that the nominal AMSR-E wind speed rmse of 0.86 m/s translates to almost 1:1 in the observed std(σ^0) via $d\sigma^0/dw$, suggesting that most of this residual variability stems from the w retrieval uncertainty; however, more in-depth analysis of the two data sets should be performed to establish that this is, in fact, the case. Moreover, the larger variability of std(σ^0) for extreme SST visible in the middle panel is due to smaller sample populations available for those conditions. The lower panel shows $\langle\sigma^0\rangle$ as function of SST for different wind speeds (color coded); a good agreement is found with the dependence of the Fresnel coefficient predicted by the model [24] both for distilled water and for SW (normality set at 35).

The σ^0 predicted by (8) using the models discussed in [12] are shown in the top panel of Fig. 2. The model by Cox and Munk (CM) [35] for nonslick surfaces was used for mss$_\lambda$ together with the standard Fresnel coefficient for water at 25 °C (generated according to Klein and Swift [24]). The CM model modified as suggested in Li *et al.* [12] (CL) is the same as CM but with the coefficient C_λ set at 0.88. In the Freilich and Vanhoff (FV) [15] and Wu [36] models for mss$_\lambda$ the same ρ_λ as in CL is adopted. Freidlich and Challenor nadir model (FC) [37] was obtained by fitting Geosat altimeter data. In general, we observe that the wind dependence at W-band is very well captured by CM, CL, and Wu but not by FV and FC. We must point out that a fit TRMM PR data better than that given by the FV curve is also obtained in [15] by accounting for wind dependence in ρ_λ so that a curve very close to FC is obtained. The two models FC and FV are representative of the Ku-band σ^0 behavior; neither matches CPR's W-band

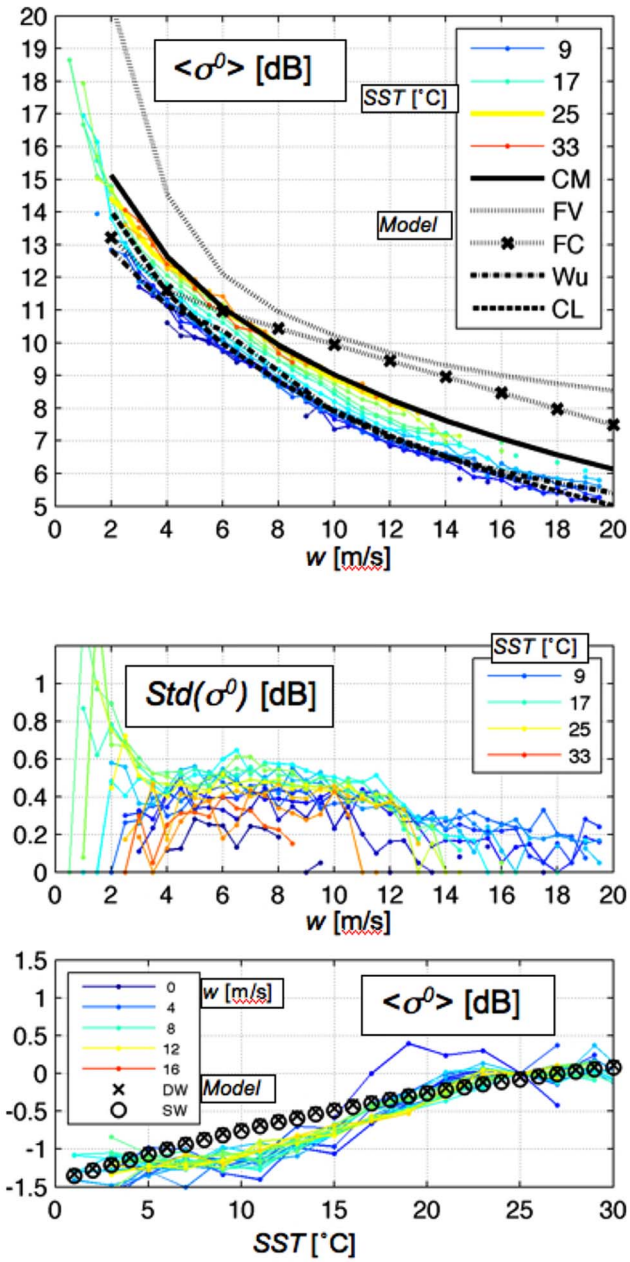

Fig. 2. CPR corrected σ^0 at nadir. (Top) Mean. (Middle) Standard deviation. (Bottom) SST dependence.

observations as well as CM, CL, or Wu which were obtained from optical observations and are therefore more representative of the full height spectrum. One possible explanation for this is that given CPR's $\lambda = 3$ mm, only a negligible portion of the height spectrum belongs to wavenumbers beyond k_λ so that (10), calculated with $k_\lambda \to \infty$, leads to a very similar result.

This interpretation, however, suggests also that C_λ for the W-band should be larger than C_λ for the Ku-band due to reduced diffractive effects. On the other hand, a W-band C_λ that is extremely similar to the one reported in [15] for the Ku-band is reported in [12]; however, the same authors clearly point out that "no conclusion should be drawn about this apparent wind-independence" due to the underlying uncertainties in calibration and corrections. CPR data, segregated by SST, seem

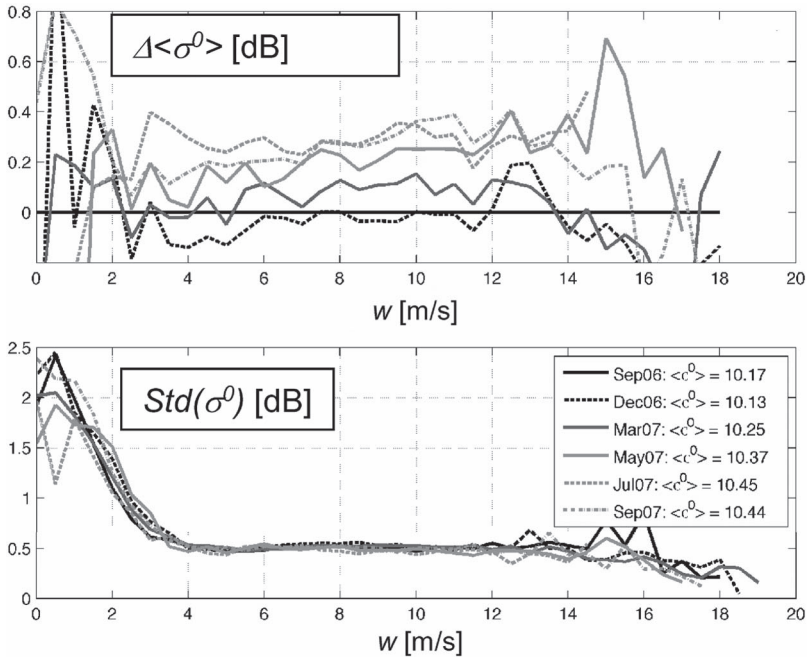

Fig. 3. Long-term trend of $\langle\sigma^0\rangle$ and std(σ^0) as function of w.

to offer one possible explanation to reconcile that result; in [12], the Fresnel coefficient for water at 20 °C is used, whereas historical data seem to suggest that an SST between 26 °C and 31 °C characterized their experiment (measurements were taken in the summer of 2002 over tropical waters around Florida and in the Gulf of Mexico). Both the modeled and the observed SST dependences suggest that this should account for about 0.5 dB, hence indicating that the bias observed in [12] could be explained by C_λ between 0.93 and 0.95, significantly larger than the Ku-band value of 0.89 found in [15].

Further analysis of the bottom panel in Fig. 2 shows that, in first approximation, the SST dependence is not correlated to the wind speed and is in good agreement with the Fresnel coefficient dependence predicted by Klein and Swift [24]. Although the observed dependence could be partially due to errors in correcting for L_a, such a contribution is expected to be minor because of the following: 1) only profiles with an estimated $L_\mathrm{a} < 2$ dB were used, and 2) the dependence appears to be at its weakest for high SST, where the $|dL_\mathrm{a}/d\mathrm{SST}|$ sensitivity is, instead, strongest (from Clausius–Clapeyron).

In order to assess the CPR end-to-end stability, analysis of σ^0 at nadir was performed for six periods between September 2006 and September 2007. The comparison of the mean σ^0 for SST between 24 °C and 28 °C is shown in the top panel of Fig. 3. The mean σ_0 from the September 2006 period is used as a baseline (i.e., it is subtracted from all mean values). A long-term fluctuation on the order of 0.3 dB is visible as a wind- and SST-independent offset. Such fluctuation shows the same magnitude and a correlation of -0.97 with the reported orbitally averaged P_t. This result indicates that the reported fluctuation of P_t is mainly determined by a fluctuation in the coupling L_c and not by a true fluctuation in the transmitted power. Considering that data processing uses P_t to calculate (1) and (4), it follows that the R04 reflectivity and σ^0 data are affected by an artificial fluctuation (of $\sim$0.4 dB as of May 2008). The L1B and L2B processing algorithms will be updated for the next release of data products to remove this artifact.

C. Monthly Calibration Maneuvers 10° Off-Nadir

The end-to-end calibration of CPR is routinely (i.e., monthly) evaluated by analyzing cloud-free clear ocean backscatter measurements. The ocean normalized radar cross section σ^0 at the Ku-band (14 GHz) is known to have a minimum sensitivity to wind speed and wind direction at approximately 10°, and several spaceborne Ku-band scatterometers and the TRMM PR have used ocean surface backscatter measurements acquired at $\sim$10° incidence angles to successfully validate their radar calibration [13], [16]. Recent airborne radar measurements also confirmed that the ocean surface backscattering coefficient is relatively insensitive to surface wind conditions near the 10° incidence angle even at 94 GHz [12]. Between August 2006 and December 2007, the CloudSat spacecraft has steered, 13 times, the CPR antenna 10° to the left or right of the orbital plane, over preselected cloud-free oceanic areas and outside the cones of exclusion defined by radio astronomy sites. The incidence angle resulting from the Earth's curvature is close to 11.1°, and the acquisition lasts 5 min.

The result of the calibration maneuvers is shown in Fig. 4, with the estimated σ^0 after all corrections binned by the wind speed ws (ws is estimated by AMSR-E with a nominal 0.86-m/s rmse). The values estimated in low water-vapor conditions are shown in Fig. 4(a) by the thick solid black curve and dots. The overall mean is shown as a thick black curve; the bias relative to the low-L_a estimates is $+0.3$ dB. This bias provides a measure of confidence on the accuracy of L_a corrections and, more generally, of the accuracy of the atmospheric attenuation profiles included in the L2B-GEOPROF product. The bars indicate the number population of valid samples for each wind bin; the largest numbers are in the range of w between 6 and

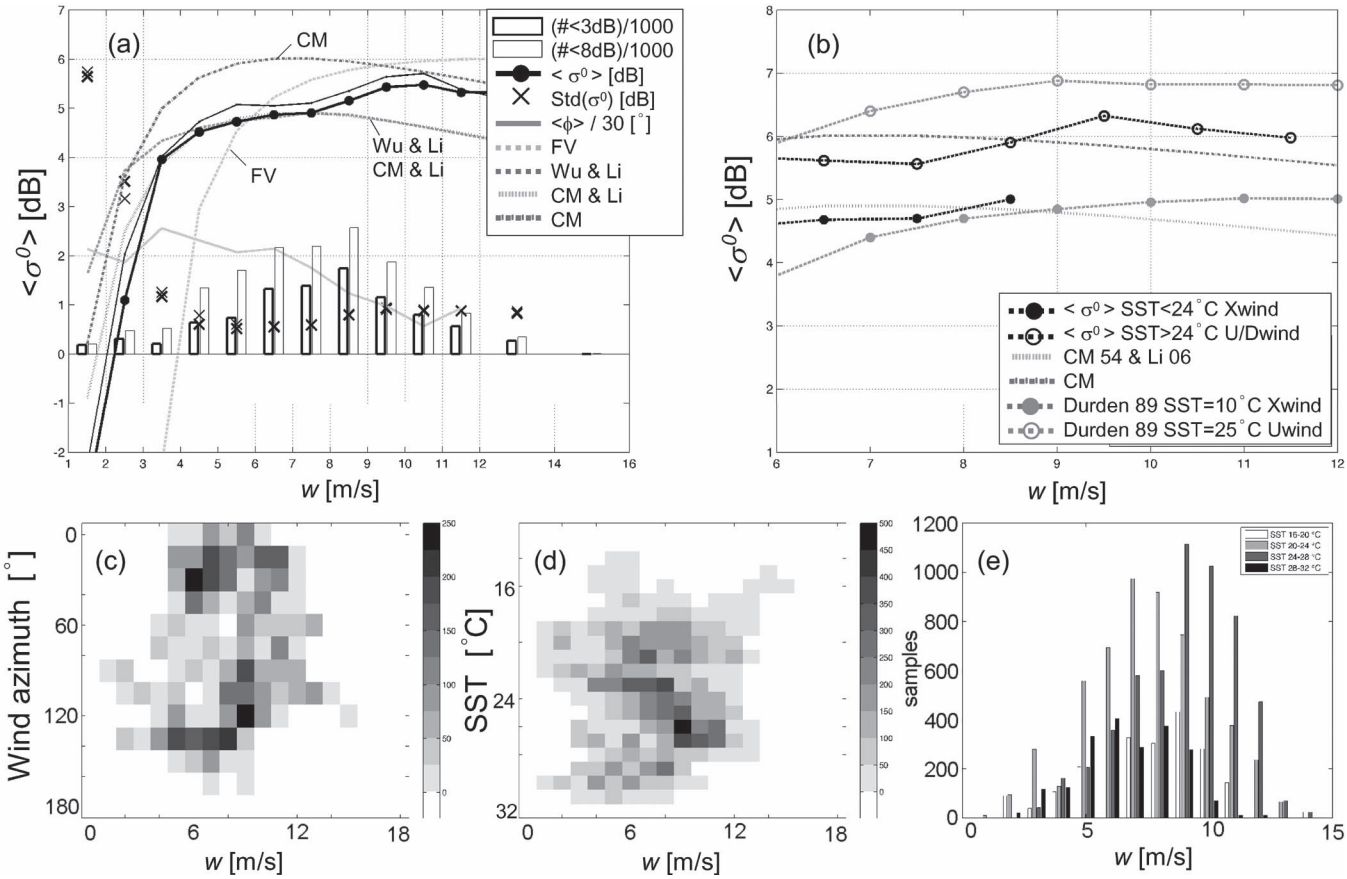

Fig. 4. CPR 10° calibration maneuvers. (a) Statistics of corrected σ^0 observed by CPR at 11.1° incidence angle versus modeled results. (b) Envelope of the uncertainty of σ^0 due to dependence on wind azimuth and SST. (c)–(e) Joint histograms characterizing the sample population used to generate (a) and (b).

10 m/s, whereas the statistics for $w < 4$ and $w > 12$ m/s should be interpreted with caution, given the small sample populations. More details on the joint distributions characterizing the sample population used to generate these results are provided in Fig. 4(c), (d), and (e). The lowest std(σ^0) is observed between 6 and 8 m/s; std(σ^0) climbs rapidly to large values for low winds as a consequence of the high $|d\sigma^0/dw|$ sensitivity, and it shows a small increase for winds above 8 m/s. The increase of std(σ^0) for $w > 8$ m/s can be attributed to an increased sensitivity to wind azimuth with a larger w.

Comparison with results obtained by the models discussed in the previous section shows excellent agreement with the CM and Wu models. CPR measurements confirm that σ^0 at the W-band and around 10° incidence angle is almost insensitive to wind velocity for wind speeds above 4 m/s. In addition, the absolute value of $\langle\sigma^0\rangle$ for $w \sim 8$ m/s is 5 dB, which is consistent with the modeled values. While the residual uncertainties in the measurement and in the correction of L_a limit the accuracy of this estimate of the std(σ^0) of less than 1 dB, estimates of the predicted value itself span more than 1 dB based on the discussed models alone.

The noticeable increase in $\langle\sigma^0\rangle$ for $w > 8$ m/s, with respect to the CM curve, is most likely due to the fact that the sample population for a large w happened to include a larger number of down- or up-wind cases than that for low-wind cases. This conclusion is supported by the average relative wind-azimuth curve shown in Fig. 4(a) by the light-gray curve; an average of about 120° was calculated for $w < 8$ m/s, whereas an average of less than 30° corresponds to a higher w. Wind-azimuth estimates were obtained from 1° that the National Centers for Environmental Prediction reanalysis fields generated for times usually within 20 min of the time of acquisition. The sample population was further binned by the wind azimuth for the most populous (w, SST) bins to reveal an up- to cross-wind modulation of about 1.5 dB. While the accuracy of this estimate is limited by residual sample populations and uncertainties in the ancillary data, it is comforting that it is qualitatively consistent with experimental findings at lower frequencies (see, e.g., [12], [14]). Wind-azimuth dependence at the W-band is beyond the scope of this paper; however, further assessment of these results was performed by comparing the measurements with the output of a two-scale sea surface backscatter model described in [27] and further modified in [38] and hereinafter referred to as Durden Vesecky (DV). Contrary to (8) and the models used in [12], DV explicitly accounts for the wind azimuth. The result of this analysis is shown in Fig. 4(b); CPR measurements from the range of w between 6 and 12 m/s were divided in cold- and warm-water cases, and the respective $\langle\sigma^0\rangle$ are shown as solid black and empty circles. The CM and CL curves are shown as reference, together with two curves from DV—one for cold water and cross wind and one for warm water and up wind. Overall, the two DV curves bracket the observations, as expected. However, the model does not capture the wind dependence as well as the CM curve. In fact, DV

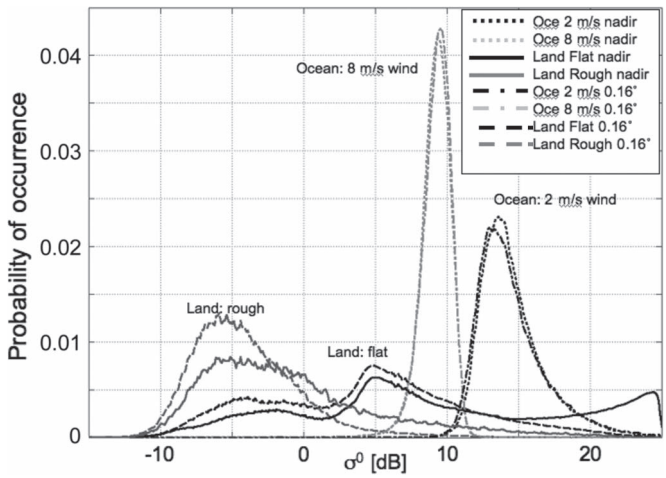

Fig. 5. CPR observed σ_0 for four surface categories. Compare nadir pointing (epoch 02) and 0.16° off-nadir pointing (epoch 03).

was developed for lower frequency applications and validated with C- and Ku-band measurements. Although the underlying theoretical framework allows for expansion to other frequencies in a consistent manner, its application to the W-band is not yet mature. Therefore, this analysis should be considered preliminary and limited in scope to the quality assessment of the data used for CPR external calibration. Comparison with other advanced models such as in [39] is planned for a future work.

The results obtained in this section were calculated based on CPR prelaunch system calibration. Based on the presented results, no change in the absolute calibration has been implemented in the L1B code.

VI. CPR Performance

A. Pointing

Three epochs exist to date, namely, June 2, 2006 through July 7, 2006, when the radar was pointing at about 1.6° off-nadir, July 7, 2006–August 15, 2006, when the pointing was set to geodetic nadir, and August 15, 2006–present, when the radar has been set to point 0.16° off-nadir to reduce the strength of the surface return as requested by the CloudSat Science Team. In fact, the CPR narrow beamwidth, combined with the pointing at geodetic nadir (i.e., orthogonal to the Earth's surface, or more precisely, to the reference ellipsoid WGS84), resulted in frequent occurrences of specular return to be observed over flat and wet regions of the Earth. Despite these differences, data acquired in the standard data-acquisition mode are broadly referred to as "nadir" data.

Fig. 5 shows the histogram of observed σ^0 for four categories of surface during two periods, namely, August 1–15, 2006, and August 16–31, 2006, representative of the "true nadir" and of the "0.16° off" periods, respectively. In the "true nadir" period, the observed σ^0 over 28% of flat land exceeded 15 dB, and over 17%, it exceeded 20 dB. The shape of the distribution curve above 15 dB is due to the presence of a specular return. The compression at 25 dB is only due to the saturation point of the CPR receiver; true values are likely to have exceeded this value. By positioning the antenna pattern null on the geodetic nadir direction, quasi-specular returns were reduced significantly (e.g., only 7% of flat land resulted in σ^0 above 15 dB, and only 1% above 20 dB), and the resulting distribution curve is more consistent with the quasi-specular return. As shown in Fig. 6, large changes (e.g., > 10 dB) in σ^0 were observed throughout the land-covered portion of the globe, with the exception of all desert and frozen regions not subject to melting during the Arctic summer of 2006. Profiles classified over rough land (i.e., SurfaceClutter_$\mathrm{Index} > 2$) were also affected; a long tail of large σ^0 values (possibly due to flat portions within the footprint) disappeared after the pointing adjustment. Much smaller effects were observed over oceanic profiles; in this case, Fig. 5 also shows the distributions of clear air σ^0 corrected for attenuation as described earlier and for two wind regimes—the 2 ($\pm$1)- and the 8 ($\pm$1)-m/s regimes. The before/after distributions show only minor changes. In both regimes, the mean σ^0 changed by less than 0.1 dB; a small drift toward lower σ^0 values can be observed for the 2-m/s regime, suggesting that some minor contribution from specular scattering may have influenced the measurements during the nadir period. However, such a change can also be explained through quasi-specular theory by accounting for the uncertainties in wind estimates and σ^0 measurements and the high wind sensitivity of σ^0 to wind speed in the low wind region as discussed in the previous section. These results confirm that the CPR pointing accuracy is accurate to at least 0.16°.

Geolocation errors can arise from a combination of pointing errors, geolocation calculations, errors in the navigation data, or errors in the time tagging of profiles. Assessment of the overall accuracy in CPR geolocation has been performed by correlating two CPR observables to digital elevation model (DEM) information. First, the long-term averages of the difference between the last profile over land and the first profile over ocean for areas of $0.25^\circ \times 0.25^\circ$ were contrasted, showing a consistently negative bias for coastlines characterized by low reflective properties (e.g., dry high coastlines) and a consistently positive bias for coastlines characterized by high reflectivity (e.g., wetland). A more accurate result was obtained by analyzing the correlation between the CPR-estimated $(r_{\mathrm{surf,CPR}})$ and DEM-estimated $(r_{\mathrm{surf,NAV}})$ ranges to the surface; the DEM used for this analysis is the GTOPO30 (data available from USGS/EROS, Sioux Falls, SD. [40]) included in CPR data products. The most refined result was generated by a reduced data set of nine granules, which has been reprocessed by introducing an artificial pointing error of $n * 0.04^\circ$, $\mathrm{n} = -2, \ldots, 2$ (corresponding to multiples of 0.5 km offset at the surface, both in the along- and cross-track directions). The best overall correlation between the CPR- and DEM-estimated ranges is found for the official L1B product. All "perturbed" products corresponding to 1 km or more of geolocation errors show residual rmse at least 40% higher than the nominal product. Of the four "perturbed" pointings at a 500-m distance, one (i.e., 500 m to the right of the line of flight) shows the smallest increase in rmse (i.e., about 10%). Given the 1-km resolution of the DEM, no further conclusion can be drawn from this result other than that the CPR geolocation is accurate within 500 m. Further tests with higher resolution DEMs are planned to improve the assessment of the CPR geolocation accuracy.

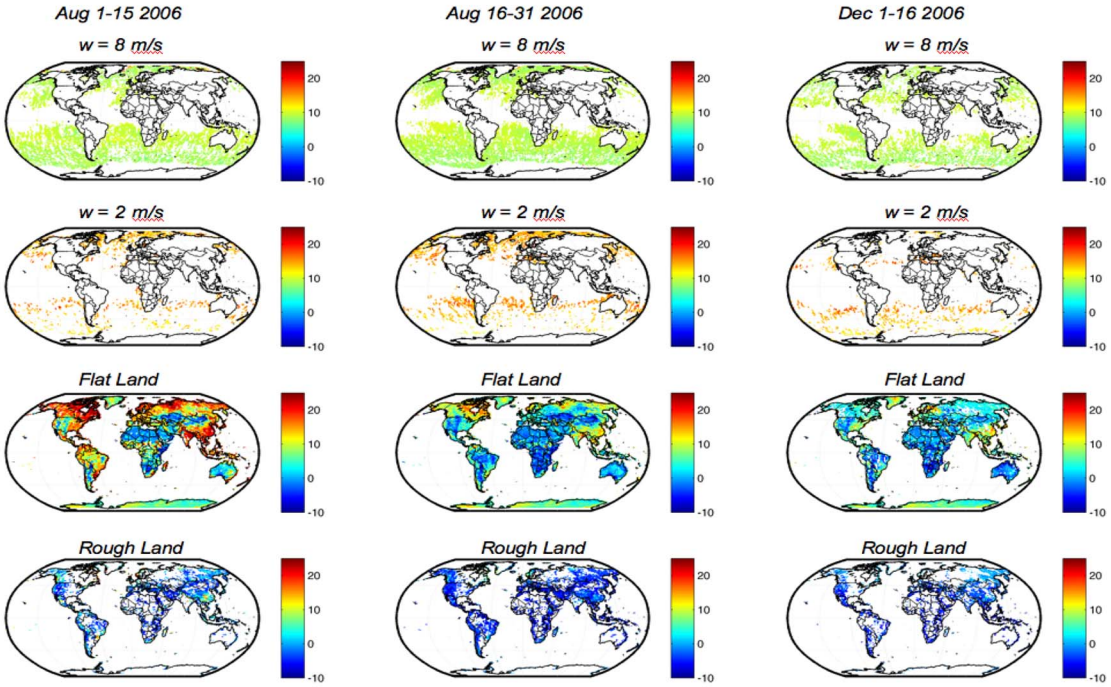

Fig. 6. CPR observed σ_0 for four surface categories. Comparison between the nadir pointing (epoch 02) and 0.16° off-nadir pointing (epoch 03); the most evident change is in the return from flat wetland. Seasonal variability is also shown by comparison of the August 16–31 period with the December 1–16 period.

B. Minimum Detectable Reflectivity Factor

The minimum detectable reflectivity factor $Z_{\min}$, is defined as the cloud reflectivity factor Z_{e}, which, after averaging and noise subtraction, yields a power equal to the noise power standard deviation. Atmospheric attenuation is not included; where present, it increases the minimum detectable reflectivity relative to that specified for CPR. $Z_{\min}$ is therefore determined by the equivalent noise floor Z_{n} and by the number of transmitted pulses.

For CPR, Z_{n} depends on the radiometric temperature of the observed scene at the W-band; the range of variability between a cold (e.g., clear air over ice at nighttime) and a hot scene (e.g., clear air over dry land desert during daytime) is of about 0.75 dB. Fig. 7(top) shows, as examples, two global maps of clear-air CPR noise-floor averages in the Arctic summer and winter. In the lower panels, the difference of the noise-floor level for two classes of cloudiness (as classified by the 2B-GEOPROF algorithm), with respect to the clear air, is shown; low-level clouds consistently raise the noise-floor level over oceanic background, whereas the effect of high-level clouds is extremely variable depending on the microphysics of the observed cloud (ice scattering depression has been observed over convective cells, whereas the presence of multilayered clouds often results in a warming effect at the W-band). The other factor contributing to $Z_{\min}$, the number of transmitted pulses, varies as a (nonlinear) function of the spacecraft altitude from a minimum of 579 to a maximum of 677, hence resulting in a further modulation of about 0.35 dB.

Overall, the CPR single-beam $Z_{\min}$ has been observed to vary by about 1 dB over the globe, as shown in the example in Fig. 8. The example shown is representative of the CPR's performance; based on the current calibration, the minimum

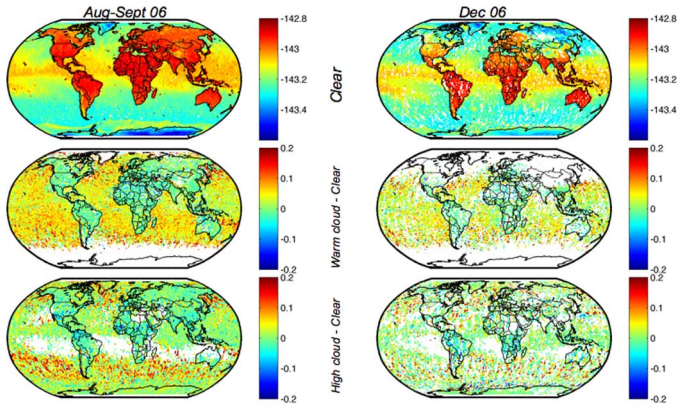

Fig. 7. CPR radiometric observations and noise-floor variability.

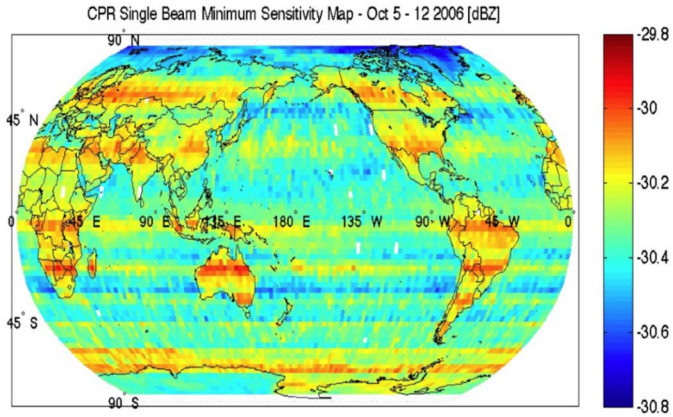

Fig. 8. CPR minimum detectable reflectivity factor observed in the period from October 5–12, 2006.

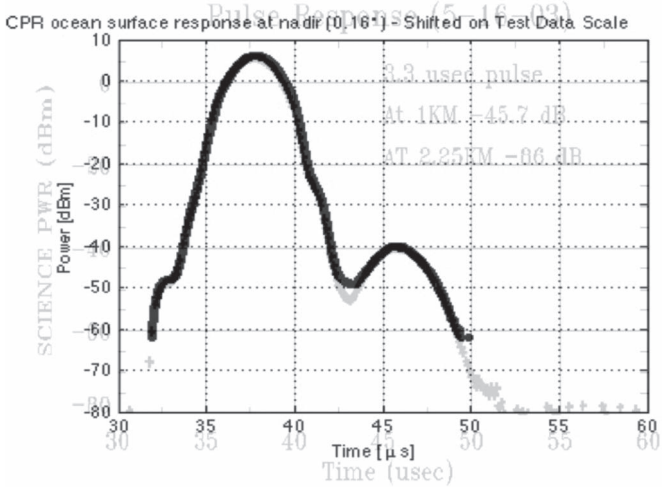

Fig. 9. CPR Ocean Surface response as function of time. (Solid black) Reconstructed from CPR in-flight science data. (Light gray) Prelaunch.

detectable reflectivity factor ranges from -29.9 to -30.9 dBZ. Seasonal changes in temperature, land cover, and sea ice, as well as cloud-cover conditions, affect the distribution of $Z_{\min}$ to a lesser order. The latitudinal banding is due to the number of transmitted pulses, which is bound to the orbital shape.

C. Range Resolution

The radar range resolution has been verified by reconstructing the point-target surface response from ocean returns in clear-air conditions. As the radar changes altitude with respect to the Earth's surface, it is possible to extract a sequence of profiles where the actual position of the Earth's surface with respect to the closest time of sampling varies with continuity at a predictable pace. Once local variations of σ^0 are removed by averaging multiple series, the shape of the ocean surface response can be compiled at a resolution much higher than the radar range resolution. For this analysis, the sampling was chosen to be 1/100th of the range-sampling distance (i.e., 2.4 m). The resulting surface response $(P'_{\rm surf})$ was compared with the point-target response measured during prelaunch tests [41]; the CPR in-flight surface response and prelaunch point-target response are shown in Fig. 9 in black and light gray, respectively. There is no significant difference other than in the regions where the noise-floor contribution becomes relevant. The 6-dB point of the surface target response is at 489 m, which reflects the fact that the Earth's surface seen by CPR at the 0.16° incidence angle is not precisely a point target (but rather a target distributed in a range of less than 10 m). The performance of the SCE technique described in the Appendix depends mainly on the accuracy of $P'_{\rm surf}$; therefore, one of the outputs of SCE has been used to test the quality of $P'_{\rm surf}$, namely, $F_{\rm r}$ the fraction of $\Delta_{\rm r}$ between the surface position and the time of sampling for the range bin $i_{\rm surf}$. In order to assess the accuracy of SCE in estimating $F_{\rm r}$, we calculate two quantities

$$R_{\rm surf,CPR} = R_0 + (i_{\rm surf} + F_{\rm r})\Delta_{\rm r} \tag{11}$$

$$R_{\rm surf,NAV} = R_{\rm intercept} - h_{\rm DEM} \tag{12}$$

where R_0 is the range to the first (i.e., top) radar bin determined by the radar timing parameters, $R_{\rm intercept}$ is the distance to the intercept to the reference ellipsoid WGS84 calculated from navigation data, and $h_{\rm DEM}$ is the DEM height at 1-km resolution from GTopo30. Over ocean, $h_{\rm DEM}$ is set to zero. Fig. 10 shows the difference between $R_{\rm surf,CPR}$ and $R_{\rm surf,NAV}$ over ocean and clear air, as a $1^\circ \times 1^\circ$ average map. Comparison with the WGS84 Geoid Anomaly shows excellent agreement; over most of the globe, an offset of only 13 m and an rmse of less than 3 m are calculated. While the offset, along with some intriguing departures such as the one visible in the Pacific warm pool, may bear useful information, it is well below what may have been expected from a radar with an intrinsic resolution of 485 m. The residual rmse of 2.5 m provides the measure of performance of the surface clutter rejection ratio (SCR) resulting from the application of the SCE algorithm; considering that $|dP'_{\rm surf}/dr|$ is always less than 0.1 dB/m (see Fig. 9), the 2.5-m rmse in the positioning of the center corresponds to a maximum SCR of 11 dB or better, depending on $F_{\rm r}$. This assessment was confirmed by the preliminary tests of L2B-GEOPROF [7].

Localized large $\mathrm{GA_{CPR}}$ (up to 800 m) are observed over land but are attributed to inaccuracies included in the DEM. In the case of Greenland, for example, comparison to a third DEM (the one generated by the ASTER instrument) confirms that CPR surface ranging is not affected by unexpected errors over land. Rather, improvements to the DEM could be implemented in the future.

VII. Current Status

CloudSat was launched on April 28, 2006; science data have been collected nearly continuously since June 2, 2006. There are a few intervals with several days of missing data starting on September 26, 2006, March 15, 2007, April 12, 2007, January 18, 2008, and May 23, 2008, which were initiated by the spacecraft computer in response to anomalous conditions either in the spacecraft bus (the first two, and the latter) or in the radar system (the other two). None of them had consequences on the spacecraft and radar function and performance, and the system was brought back to full operation in all instances. Several others amount to a few minutes each and are mainly related to planned spacecraft maneuvers needed to either perform the monthly calibration maneuvers or to maintain the integrity of the A-train by compensating for atmospheric drag and by adjusting the orbit in response to orbital maneuvers by Aqua or Calipso.

As of the time of writing (May 2008), CPR has completed its primary mission and has entered an extended mission phase. It is fully functional and performing beyond requirement.

VIII. Summary

The CPR for the CloudSat mission is a 94-GHz nadir-pointing high-power pulse radar. It is the first-ever millimeter-wave, and the most sensitive, atmospheric radar launched into space. Its -30-dBZ detection sensitivity is enabling the first global view of cloud and precipitation vertical structure at a 500-m resolution. The data acquired by the CloudSat radar are stimulating important new research on clouds and precipitation and, together with the A-Train, provide a unique opportunity to advance our understanding of the aerosol effects on clouds and

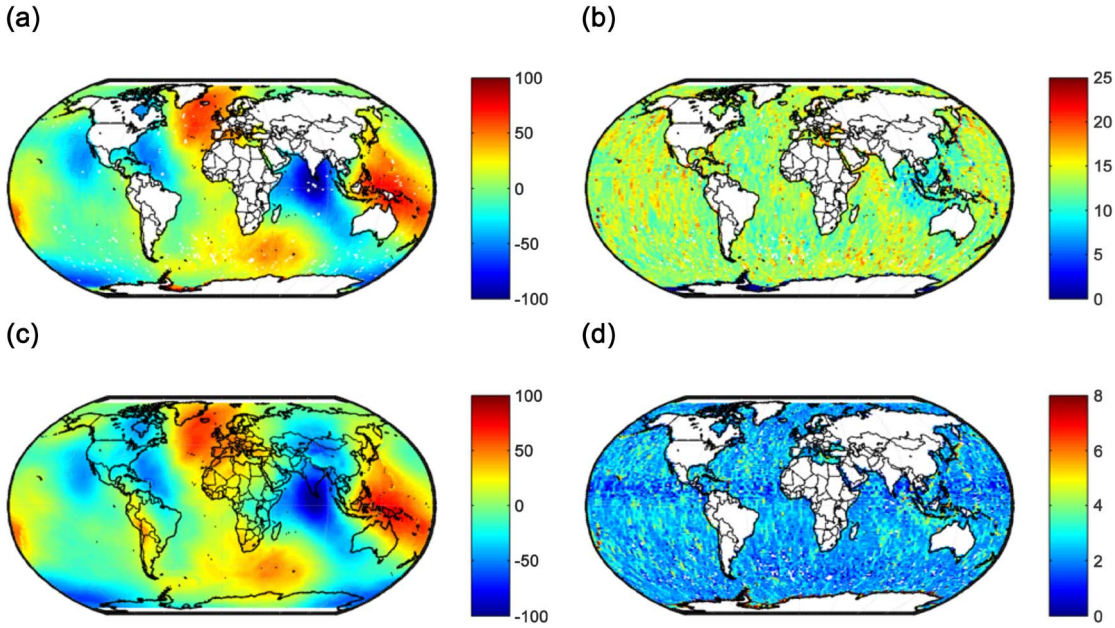

Fig. 10. CPR detection of the Geoid Anomaly (in color in the electronic version). (a) $\mathrm{GA_{CPR}} = R_{\mathrm{surf,CPR}} - R_{\mathrm{surf,NAV}}[m+13]$. (b) $\mathrm{GA_{CPR}}-$WGS84 Geoid Anomaly $[m]$. (c) WGS84 Geoid Anomaly $[m]$. (d) Std $\mathrm{GA_{CPR}}[m]$.

precipitation. The CloudSat mission also provides an important demonstration of the 94-GHz radar technology in a spaceborne application. We have provided an overview of this new radar and have described how radar calibration and stability have been verified by analyzing sea surface backscatter in clear air and how surface backscatter is estimated and corrected in CloudSat's data processing.

Appendix A
SCE and Correction for Range-Sampling Bias

CPR data products are contaminated by ground clutter in the lower 1 km of the atmospheric profile. This level of contamination was expected as a result of tradeoffs in the design of the radar system. However, there is high interest in the scientific community to mitigate the effect of surface clutter in order to study low clouds and light rainfall at altitudes as close as possible to the Earth's surface. The first algorithm capable of reducing the effect of surface clutter in CPR data has been developed at JPL and included in the R04 of CloudSat data products. The technique is based on three steps, where first, the in-flight surface response is reconstructed at a resolution higher than CPR's intrinsic resolution $\Delta_{6\,\mathrm{dB}}$; second, such surface response is used in a conventional maximum correlation scheme to estimate the level of surface clutter contamination at each position in the radar profile; and finally, the estimated surface clutter profile is removed from the measured profile. For R04, the first step has been performed only for flat surfaces in epoch 03; therefore, the second (implemented in L1B) and third (implemented in L2B-GEOPROF) steps are optimized only for flat surfaces in epoch 03.

CloudSat's orbit is such that its geodetic altitude varies continuously over a range of approximately 25 km. As the geodetic altitude changes, the radar timing parameters are changed at intervals defined by the flight software in order to keep the Earth's troposphere inside the data-collection window. Within each interval, the surface continuously "scans through" (i.e., it moves across) a few range bins of the data window. For each radar profile, samples are acquired every 1.6 μs (corresponding to $\Delta_{\mathrm{r}} \sim 240$ m). As shown in Fig. 7, the mainlobe of the point-target response lasts for about 12 μs; therefore, about eight samples of the surface clutter signature are available around the range bin i_{surf} where the peak of surface return is observed. Samples in consecutive radar profiles are slightly (i.e., $\ll \Delta_{\mathrm{r}}$) offset with respect to each other according to the relative change in the geodetic altitude. It follows that a sequence of consecutive profiles, gathered over a homogeneous surface, carries samples of the surface response with a much higher resolution than the original. The high-resolution surface response $P_{\mathrm{surf}}(m)$, in decibels, at a resolution $\Delta\rho = \Delta_{\mathrm{r}}/M$ was calculated for flat surfaces by rearranging a set of 3000 clear ocean surface responses from CPR, and stored for use in the following steps.

Once the high-resolution surface response is available, the profile of surface clutter can be accurately estimated by a conventional maximum correlation scheme; a translated and scaled version of the high-resolution surface response is fitted to the observed low-resolution profile. The translation and scaling factors that optimize the fit in a maximum correlation sense represent the surface true position relative to the sampled surface peak and the magnitude of the surface backscatter

$$(m_{\mathrm{fit}}, K_{\mathrm{fit}}) = \min_{j,K} \left\{ \sum_{i=i_{\mathrm{surf}}-N_{\mathrm{SC1}}}^{I_{\mathrm{surf}}+N_{\mathrm{SC2}}} \left[P_{\mathrm{m}}(i) - P_{\mathrm{e}}(i, i_{\mathrm{surf}}, m, K)\right]^2 \right\} \tag{13}$$

where P_{m} is the observed profile, in decibels, at the nominal sampling resolution; i is the range bin; and P_{e} is the decimated, translated, and scaled P_{surf}

$$P_{\mathrm{e}}(i, i_{\mathrm{surf}}, m, K) = K + P_{\mathrm{surf}}\left[m + M(i = i_{\mathrm{surf}})\right]. \tag{14}$$

The value of the functional in (10) calculated for the best fit parameters is reported in the L1B product as the Surface-Clutter_Index ($C_{\rm I}$). Once the high-resolution surface response that best fits the data is identified in this manner, the following parameters are calculated:

$$10\log_{10}(L_{\rm r}) = P_{\rm surf}(m_{\rm max}) - P_{\rm surf}(m_{\rm fit}) \quad (15)$$

$$F_{\rm surf} = (m_{\rm max} - m_{\rm fit})/M \quad (16)$$

where $P_{\rm surf}(m_{\rm max}) = \max P_{\rm surf}(m)$, $F_{\rm surf}$ is the SurfaceBin-Number_Fraction reported in L1B data, and $L_{\rm r}$ is the range-sampling bias used in L1B to correct the measured σ^0. It must be pointed out that the measured σ^0 is only corrected for $L_{\rm r}$ and not for $L_{\rm a}$ or L_θ. Correction for $L_{\rm r}$ is disabled for profiles where $C_1 > 2$. Furthermore, considering that the SCE algorithm is implemented in L1B and, therefore, prior to noise subtraction and cloud masking (which occur in L2B-GEOPROF), very low values of σ^0 (e.g., below -20 dB) are significantly affected by the contribution of the noise floor (at about -46 dB σ^0-equivalent) and, occasionally, by the presence of signal generated by hydrometeors (be it from single scattering from surface rain or multiple scattering from higher altitude bins). Profiles that are significantly affected by such contributions are identified by large values of $C_{\rm I}$ (e.g., $C_{\rm I} > 10$), and caution should be exercised when interpreting the reported σ^0 values in these cases.

ACKNOWLEDGMENT

The research described in this paper was performed at the JPL, California Institute of Technology, under contract with the NASA.

The authors would like to thank C. Saldana for his support in the daily processing of CloudSat's data and the implementation of the state of health analysis package.

REFERENCES

[1] G. L. Stephens *et al.*, "The CloudSat mission and the A-Train," *Bull. Amer. Meteorol. Soc.*, vol. 83, no. 12, pp. 1773–1789, Dec. 2002.

[2] E. Im, C. Wu, and S. L. Durden, "Cloud profiling radar for the CloudSat mission," in *Proc. IEEE Radar Conf.*, May 9–12, 2005, pp. 483–486.

[3] E. Im, S. Tanelli, S. L. Durden, and K. S. Pak, "Cloud profiling radar performance," in *Proc. IEEE Int. Geosci. Remote Sens. Symp.*, Jul. 23–28, 2007, pp. 5061–5064.

[4] R. Meneghini, J. A. Jones, and L. H. Gesell, "Analysis of a dual-wavelength surface reference radar technique," *IEEE Trans. Geosci. Remote Sens.*, vol. GRS-25, no. 4, pp. 456–471, Jul. 1987.

[5] J. H. Haynes, T. S. L'Ecuyer, G. L. Stephens, S. D. Miller, C. M. Mitrescu, and S. Tanelli, "Rainfall retrieval over the ocean using spaceborne high-frequency cloud radar," *J. Geophys. Res.* to be published.

[6] L. Li, S. L. Durden, and S. Tanelli, *Level 1B CPR Process Description and Interface Control Document Version 5.3*, 2007. [Online]. Available: http://www.cloudsat.cira.colostate.edu

[7] G. Mace and R. Marchand, *Level 2 GEOPROF Product Process Description and Interface Control Document Algorithm Version 5.3*, 2007. [Online]. Available: http://www.cloudsat.cira.colostate.edu

[8] J. R. Probert-Jones, "The radar equation for meteorology," *Q. J. R. Meteorol. Soc.*, vol. 88, pp. 485–495, 1962.

[9] F. T. Ulaby, R. K. Moore, and A. K. Fung, *Remote Sensing: Active and Passive*, vol. 3. Norwood, MA: Artech House, 1981. 465 pp.

[10] R. Meneghini and T. Kozu, *Spaceborne Weather Radar*. Norwood, MA: Artech House, 1990. 199 pp.

[11] C. Kummerow *et al.*, "The status of the Tropical Rainfall Measuring Mission (TRMM) after two years in orbit," *J. Appl. Meteorol.*, vol. 39, no. 12, pp. 1965–1982, Dec. 2000.

[12] L. Li *et al.*, "Measurements of ocean surface backscattering using an airborne 94-GHz cloud radar—Implication for calibration of airborne and spaceborne W-band radars," *J. Atmos. Ocean. Technol.*, vol. 22, no. 7, pp. 1033–1045, Jul. 2005.

[13] L. Li, E. Im, S. L. Durden, and Z. S. Haddad, "A surface wind model-based method to estimate rain-induced radar path attenuation over ocean," *J. Atmos. Ocean. Technol.*, vol. 19, no. 5, pp. 658–672, May 2002.

[14] S. Tanelli, S. L. Durden, and E. Im, "Simultaneous measurements of Ku- and Ka-band sea surface cross-sections by an airborne radar," *IEEE Geosci. Remote Sens. Lett.*, vol. 3, no. 3, pp. 359–363, Jul. 2006.

[15] M. H. Freilich and B. A. Vanhoff, "The relationship between winds, surface roughness, and radar backscatter at low incidence angles from TRMM precipitation radar measurements," *J. Atmos. Ocean. Technol.*, vol. 20, no. 4, pp. 549–562, Apr. 2003.

[16] S. L. Durden, E. Im, F. K. Li, W. Ricketts, A. Tanner, and W. Wilson, "ARMAR: An airborne rain-mapping radar," *J. Atmos. Ocean. Technol.*, vol. 11, no. 3, pp. 727–737, Jun. 1994.

[17] N. Takahashi, H. Kuroiwa, and T. Kawanishi, "Four-year result of external calibration for Precipitation Radar (PR) of the Tropical Rainfall Measuring Mission (TRMM) satellite," *IEEE Trans. Geosci. Remote Sens.*, vol. 41, no. 10, pp. 2398–2403, Oct. 2003.

[18] G. A. Sadowy, A. C. Berkun, W. Chun, E. Im, and S. L. Durden, "Development of an advanced airborne precipitation radar," *Microw. J.*, vol. 46, no. 1, pp. 84–98, Jan. 2003.

[19] T. Kozu, "A generalized surface echo radar equation for down-looking pencil beam radar," *IEICE Trans. Commun.*, vol. E78B, no. 8, pp. 1245–1248, 1995.

[20] I. J. Caylor, G. M. Heymsfield, R. Meneghini, and L. S. Miller, "Correction of sampling errors in ocean surface cross-sectional estimates from Nadir-looking weather radar," *J. Atmos. Ocean. Technol.*, vol. 14, no. 1, pp. 203–210, Feb. 1997.

[21] F. Wentz and T. Meissner, *AMSR-E/Aqua L2B Global Swath Ocean Products derived from Wentz Algorithm V001*. Boulder, CO: Nat. Snow Ice Data Center, Mar.–Jun. 2004. updated daily; Digital media.

[22] H. J. Liebe, G. A. Hufford, and M. G. Cotton, "Propagation modeling of moist air and suspended water/ice particles at frequencies below 1000 GHz," in *Proc. AGARD Meeting Atmos. Propag. Effects Through Natural Man-Made Obscurants for Visible MM-Wave Radiation*, May 1993, pp. 3/1–3/11.

[23] H. J. Liebe, "An updated model for millimeter wave propagation in moist air," *Radio Sci.*, vol. 20, no. 5, pp. 1069–1089, 1985.

[24] L. A. Klein and C. T. Swift, "An improved model for the dielectric constant of sea water at microwave frequencies," *IEEE Trans. Antennas Propag.*, vol. AP-25, no. 1, pp. 104–111, Jan. 1977.

[25] T. Meissner and F. J. Wentz, "The complex dielectric constant of pure and sea water from microwave satellite observations," *IEEE Trans. Geosci. Remote Sens.*, vol. 42, no. 9, pp. 1836–1849, Sep. 2004.

[26] P. S. Ray, "Broadband complex refractive indices of ice and water," *Appl. Opt.*, vol. 11, no. 8, pp. 1836–1844, Aug. 1972.

[27] S. L. Durden and J. F. Vesecky, "A physical radar cross-section model for a wind-driven sea with swell," *IEEE J. Ocean Eng.*, vol. 10, no. 4, pp. 445–451, Oct. 1985.

[28] G. R. Valenzuela, "Theories for the interaction of electromagnetic and ocean waves—A review," *Boundary-Layer Meteorol.*, vol. 13, pp. 61–85, 1978.

[29] G. L. Tyler, "Wavelength dependence in radio-wave scattering and specular-point theory," *Radio Sci.*, vol. 11, no. 2, pp. 83–91, 1976.

[30] D. Vandemark, B. Chapron, J. Sun, G. H. Crescenti, and H. C. Graber, "Ocean wave slope observations using radar backscatter and laser altimeters," *J. Phys. Oceanogr.*, vol. 34, no. 12, pp. 2825–2841, Dec. 2004.

[31] E. J. Walsh, D. C. Vandemark, C. A. Friehe, S. P. Burns, D. Khelif, R. N. Swift, and J. F. Scott, "Measuring sea surface mean square slope with a 36-GHz scanning radar altimeter," *J. Geophys. Res.*, vol. 103, no. C6, pp. 12.587–12.601, 1998.

[32] L. C. Schroeder *et al.*, "The relationship between wind vector and normalized radar cross section used to derived SEASAT—A satellite scatterometer winds," *J. Geophys. Res.*, vol. 87, no. C5, pp. 3318–3337, 1982.

[33] L. C. Schroeder, P. R. Schaffner, J. L. Mitchell, and W. L. Jones, "AAFE RADSCAT 13.9-GHz measurements and analysis: Wind-speed signature of the ocean," *IEEE J. Ocean Eng.*, vol. 10, no. 4, pp. 346–357, Oct. 1985.

[34] F. Wentz, S. Peteherych, and L. A. Thomas, "A model function for ocean radar cross section at 14.6 GHz," *J. Geophys. Res.*, vol. 89, no. C3, pp. 3689–3704, 1984.

[35] C. Cox and W. Munk, "Measurement of the roughness of the sea surface from photographs of the sun's glitter," *J. Opt. Soc. Amer.*, vol. 144, no. 11, pp. 838–850, Nov. 1954.
[36] J. Wu, "Mean square slopes of the wind-disturbed water surface, their magnitude, directionality, and composition," *Radio Sci.*, vol. 25, no. 1, pp. 37–48, 1990.
[37] M. H. Freilich and P. G. Challenor, "A new approach for determining fully empirical altimeter wind speed model functions," *J. Geophys. Res.*, vol. 99, no. C12, pp. 25 051–25 062, Dec. 1994.
[38] F. Li, G. Neumann, S. Shaffer, and S. L. Durden, "Studies of the location of azimuth modulation minima for Ku band ocean radar backscatter," *J. Geophys. Res.*, vol. 93, no. C7, pp. 8229–8238, 1988.
[39] T. Elfouhaily, B. Chapron, K. Katsaros, and D. Vandemark, "A unified directional spectrum for long and short wind-driven waves," *J. Geophys. Res.*, vol. 102, no. C7, pp. 15 781–15 796, 1997.
[40] N. B. Bliss and L. M. Olsen, "Development of a 30-arc-second digital elevation model of South America," in *Proc. Pecora Thirteen, Human Interactions with Environ.—Perspectives from Space*, Sioux Falls, SD, Aug. 20–22, 1996.
[41] R. LaBelle, R. Girard, and G. Arbery, "A 94 GHz RF electronics subsystem for the CloudSat cloud profiling radar," in *Proc. 33rd Eur. Microw. Conf. (IEEE Cat. No.03EX723C)*, 2003, vol. 3, pp. 1139–1142.

Simone Tanelli received the Laurea (*cum laude*) degree in electronic engineering and the Ph.D. degree in environmental monitoring from the University of Florence, Florence, Italy, in 1995 and 1999, respectively.

He has been with the Jet Propulsion Laboratory (JPL), California Institute of Technology, Pasadena, since 2001. He has worked on the second-generation precipitation radar (APR-2), the CloudSat W-band Cloud Profiling Radar, and serves in the CloudSat/CALIPSO and Precipitation Measurement Missions Science Teams focusing on algorithms for precipitation and cloud parameter retrievals and calibration. He is currently a Senior Engineer with the Radar Science and Engineering Section, JPL, and is Radar Engineer for CloudSat and APR-2 operations, processing, and analysis. His research interests are in the areas of spaceborne meteorological radar science and engineering; advanced radar system and technology studies; and remote-sensing methods, technologies, and algorithms. He is the author or coauthor of more than 20 journal publications.

Dr. Tanelli is a member of the American Meteorological Society and of the International Precipitation Working Group.

Stephen L. Durden (S'82–M'86–SM'99) received the B.S. degree in electrical engineering and applied mathematics from Rice University, Houston, TX, and the M.S. and Ph.D. degrees in electrical engineering from Stanford University, Stanford, CA.

He has been with the Jet Propulsion Laboratory (JPL), California Institute of Technology, Pasadena, since 1986, where he has worked on the NSCAT ocean scatterometer project, the airborne polarimetric SAR, the Airborne Rain Mapping Radar, the Airborne Cloud Radar, LightSAR, second-generation precipitation radar, the CloudSat W-band Cloud Profiling Radar, the Extended Ocean Vector Winds Mission ocean scatterometer study, and various research tasks involving modeling and analysis of radar data. He was the Lead Systems Engineer of the CloudSat radar development and is currently a Principal Engineer with the Radar Science and Engineering Section, JPL. He is a member of the CloudSat/CALIPSO Science Team and also served on the Tropical Rainfall Measuring Mission, Precipitation Measurement Missions, and Aqua Science teams. He is the author or coauthor of approximately 60 journal publications.

Dr. Durden is member of the American Geophysical Union and of Phi Beta Kappa.

Eastwood Im (S'81–M'85–SM'01–F'06) received the B.S., M.S., and Ph.D. degrees in electrical engineering from the University of Illinois, Urbana, in 1981, 1982, and 1985, respectively.

He was the first instrument architect of the multifunctional radar for the Cassini Mission to Saturn during the preproject phase (1987–1991), and went on to become the system engineer of that instrument until its launch in 1997. He was the CloudSat radar instrument Manager from inception through the end of the first year of flight operations (1998–2007). Since 1998, he has been the Principal Investigator of several National Aeronautics and Space Administration (NASA) studies, developing new radar technologies for future spaceborne atmospheric science missions. He has also led the development of the NASA airborne dual-frequency precipitation radar and its deployment in several NASA science field experiments, including CAMEX-4 in 2001, EOS AQUA validation in 2002, NAMMA in 2006, and in TC-4 in 2007. He has been with the Jet Propulsion Laboratory (JPL), California Institute of Technology, Pasadena, since 1986, where he is currently the Manager of the Earth Science Technology Research and Advanced Concepts Office. He has been a member of NASA's Tropical Rainfall Measuring Mission Science Team and the Precipitation Measurement Missions Science Team, focusing on the studies of advanced radar techniques and algorithms for precipitation and cloud parameter retrievals and calibration. He was the Associate Editor of the American Meteorological Society *Journal of Atmospheric and Oceanic Technology* (1999–2000). He has published over 190 articles, in refereed journals and conference proceedings, and ten technical reports. His research interests are in the areas of spaceborne meteorological radar science and remote sensing and advanced radar system and technology studies.

Dr. Im is a member of the American Meteorological Society, the American Geophysical Union, and the American Institute of Aeronautics and Astronautics. His services include being an IEEE International Geoscience and Remote Sensing Symposium Technical Program Committee member and Session Chair/Cochair (1999–2007); a member of the National Research Council Committee on Evaluation of the Multifunction Phased Array Radar (2008); and the Technical Program Chair of the IEEE Radar Conference (2009). He is the recipient of the NASA's Exceptional Technology Achievement and Exceptional Engineering Achievement Medals, the JPL's Explorer Award, and the Awards of Technical Excellence.

Kyung S. Pak received the B.S. degree in physics and the M.S. and Ph.D. degrees in electrical engineering from the University of Washington, Seattle, in 1990, 1992, and 1996, respectively.

He is a Member of the Senior Technical Staff in the Radar Science and Engineering Section, Jet Propulsion Laboratory, California Institute of Technology, Pasadena. He is engaged in the study of spaceborne microwave and millimeter-wave radar performance, calibration, and science data processing. His research interests include radar environment simulation, electromagnetic wave scattering from rough surfaces, and remote sensing of the ocean and atmosphere.

Dale G. Reinke received the B.S. degree in computer science from Colorado State University (CSU), Fort Collins, in May 1993.

His expertise is in the field of data-processing software algorithms and techniques. He is an Earthstation Senior Software Engineer responsible for Cloudsat software development and Earthstation software maintenance. He is currently with the Cooperative Institute for Research in the Atmosphere, CSU.

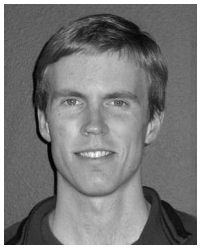

Philip Partain received the B.S. degree in atmospheric science from the University of California, Los Angeles, in 1994 and the M.S. degree in atmospheric science from Colorado State University (CSU), Fort Collins, in 1998.

He is currently with the METSAT Division, Science and Technology Corporation, Fort Collins, CO. He is also currently with the CloudSat Data Processing Center, Cooperative Institute for Research in the Atmosphere, CSU, where he is the Lead Programmer responsible for system development and operation. His research interests include atmospheric remote sensing and radiative transfer.

John M. Haynes received the B.S. degree from Pennsylvania State University, University Park, and the M.S. and Ph.D. degrees from Colorado State University (CSU), Fort Collins.

He is currently with the Department of Atmospheric Science, CSU. His research interests include the development of a light precipitation retrieval algorithm for the CloudSat radar, characterization of the properties of precipitating cloud systems, and evaluation of clouds and precipitation in numerical weather-prediction models.

Roger T. Marchand received the Ph.D. degree in electrical engineering from Virginia Polytechnic Institute and State University, Blacksburg, in 1997.

He is currently with the Joint Institute for the Study of the Atmosphere and Ocean, University of Washington, Seattle. In regard to satellite sensors, he is a member of the National Aeronautics and Space Administration CloudSat, Multiangle Imaging SpectroRadiometer, and MODIS instrument teams, and is a longtime participant in the Department of Energy Atmospheric Radiation Measurement Program. His research focuses on testing and improving the representation of clouds in climate and cloud resolving models with remote-sensing observations from millimeter-wavelength radar, lidar, and a variety of passive remote-sensing instrumentation and includes both satellites and ground-based systems.